Journal of Materials Chemistry A

Accepted Manuscript

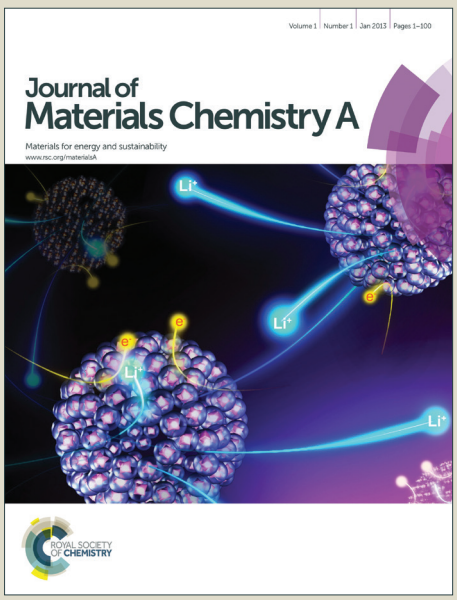

ROYAL SOCIETY OF CHEMISTRY

www.rsc.org/materialsA

Journal Name

RSCPublishing

ARTICLE

Linking Morphology with Activity through the Lifetime of Pretreated PtNi Nanostructured Thin Film Catalysts

Cite this: DOI: 10.1039/x0xx00000x

Received 00th January 2012,
Accepted 00th January 2012

DOI: 10.1039/x0xx00000x

www.rsc.org/

D. A. Cullen,[a] M. Lopez-Haro,[b] P. Bayle-Guillemaud,[b] L. Guetaz,[c] M. K. Debe,[d†] and A. J. Steinbach[d]

The nanoscale morphology of highly active Pt_3Ni_7 nanostructured thin film fuel cell catalysts is linked with catalyst surface area and activity following catalyst pretreatments, conditioning and potential cycling. The significant role of fuel cell conditioning on the structure and composition of these extended surface catalysts is demonstrated by high resolution imaging, elemental mapping and tomography. The dissolution of Ni during fuel cell conditioning leads to highly complex, porous structures which were visualized in 3D by electron tomography. Quantification of the rendered surfaces following catalyst pretreatment, conditioning, and cycling shows the important role pore structure plays in surface area, activity, and durability.

Introduction

Bimetallic and multimetallic catalysts are under intense research for use in polymer electrolyte membrane (PEM) fuel cells.[1] Replacing a portion of the costly Pt metal oxygen reduction reaction (ORR) catalyst with transition metals such as Co, Fe, or Ni can not only reduce the overall cost of the catalyst, but can also result in a structure with enhanced specific activity due to the formation of Pt-skin, -shell, or -skeleton structures.[2-4] Ongoing development of these Pt-metal catalysts aims at meeting critical cost, activity, and durability milestones.[5]

Nanostructured thin films (NSTF) developed by 3M Company are a novel extended surface electrode structure with significant advantages in specific activity, durability, and cost.[6] These advantages arise from the unique characteristics of both the catalyst and support. The organic perylene-red support does not suffer from corrosion issues that plague conventional high surface area carbon supported materials.[7] The thin-film-like geometry of the NSTF catalyst makes it less susceptible to Pt agglomeration and dissolution, a major durability concern of conventional nanoparticle catalysts. All this is accomplished at lower Pt loadings, requiring less of the costly precious metal catalyst. The performance and cost of NSTF electrodes are further improved by using a Pt-based alloy catalyst, in which a sharp peak in ORR activity has been observed for a catalyst with an initial composition approaching Pt_3Ni_7.[8] The ca. 3x gain in mass activity of the Pt_3Ni_7/NSTF over previous Pt or PtCoMn alloy NSTF catalysts is due to substantial increases in both the specific activity and specific surface area.

Based on nanoparticle and thin film research, it is expected that further stability and activity gains can be achieved by dealloying and annealing procedures performed prior to assembly into catalyst-coated membranes (CCMs).[9-11] The combination of dealloying and annealing can modify catalyst composition and surface structure, leading to significant improvements in activity and/or durability.[12] Such treatments can be used to form and control nanoporosity, the formation of which is highly dependent on particle size and composition.[3,12,13]

While these pretreatments clearly contribute to increases in fuel cell performance, drawing structure-property relationships based on the characterization of the pretreated catalyst alone can be misleading due to the often overlooked impact of fuel cell conditioning. In order to reach peak performance, a newly assembled fuel cell must typically undergo what is known as a conditioning or break-in process.[14] These conditioning protocols can vary widely in both nature and duration, spanning from a few hours to several days.[15,16] Typically, the protocol

involves some combination of constant voltage, constant current, and/or voltage cycling operation.[14] Prior to activity and surface area measurements, the pretreated catalyst undergoes the additional, and sometimes extensive, conditioning treatment. Thus, attempts to correlate structures formed during pretreatments with activity measurements performed after catalyst conditioning can be misleading due to the potential for rapid morphological changes during the conditioning process. In the case of pure Pt nanoparticle catalysts, morphological changes due to conditioning are typically limited. An *in operando* XANES study of Pt nanoparticle catalysts suggested that break-in resulted in an increase in Pt-Pt coordination number, a reflection of subtle morphological changes such as smoothing of particle edges.[17] However, in Pt-transition metal alloy systems, morphological changes during break-in can be significant due to the rapid dissolution of the transition metal in the presence of the acidic proton-conducting ionomer and membrane.[12,18] In this case, microstructural characterization of the conditioned alloy catalyst in the embedded state of the membrane electrode assembly (MEA), although much less convenient, may be critical to establishing proper structure-property relationships.

In this work, we first demonstrate significant changes in catalyst morphology during MEA conditioning of pretreated Pt_3Ni_7/NSTF cathodes. Through a combination of cyclic voltammetry and advanced electron microscopy methods, we demonstrate the critical role catalyst conditioning plays in forming the structures which promote the high activity and surface area of the Pt-Ni alloy NSTF. Changes in bulk alloy composition, formation of Pt-rich surface layers, and the emergence of nanoporosity following fuel cell conditioning were all observed. These results show that for Pt-transition metal alloy systems, it is critical to characterize the catalyst in the conditioned state if accurate structure-property relationships are to be established.

Further, the durability of the NSTF microstructure was studied after 30,000 drive cycles between 0.6 – 1V. TEM analysis shows Ni dissolution, surface smoothing, and pore growth as a result of drive cycling. In order to correlate the electrochemical properties to the microstructure parameters, the three samples - pretreated, conditioned and cycled PtNi/NSTF - were analysed using advanced scanning transmission electron microscopy (STEM) techniques including electron energy loss spectroscopy (EELS), energy dispersive X-ray spectroscopy (EDS), and electron tomography. This last technique enables 3D visualization of the nanoporosity which not only shows the size and interconnectivity of the pores but also from which the catalyst surface area and volume can be extracted. Coupled with the compositional analysis, the specific surface area of individual NSTF whiskers was determined and compared with the electrochemical measurements.

Results and Discussion

Fuel Cell Performance

High performance Pt_3Ni_7 NSTF was submitted to brief chemical dealloying and annealing protocols, as described in the experimental section. Relative to the as-grown catalyst, these pretreatments led to only a modest increase in specific activity from 2.5 to 2.7 mA/cm^2_{Pt}. This slight improvement was mitigated by a slight decrease in specific area (from 15.3 to 14.7 m^2_{Pt}/g). More substantial benefits of the pretreatment were seen in the high current density (mass transport) performance (Fig. 1a). Relative to a Pt/NSTF cathode, the as-deposited Pt_3Ni_7/NSTF cathode exhibited substantially reduced limiting current density, likely due to electrochemical dissolution of Ni from the cathode to form Ni^{2+}. The decreased limiting current density can be attributed to deleterious changes in PFSA PEM water management[19] and depletion of proton concentration within the cathode catalyst layer due to cation electromigration.[20]

Pretreatments resulted in a marked improvement in limiting current density, which is attributed to the lower Ni content of the pretreated catalyst, leading to less Ni poisoning in the membrane.

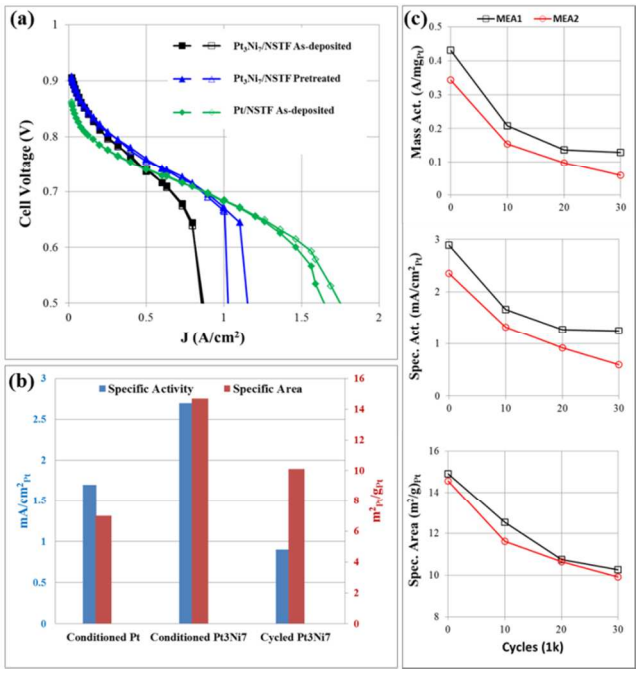

Fig. 1 (a) H_2/air polarization curves of MEAs with as-deposited and pretreated Pt_3Ni_7/NSTF cathodes with loadings of 0.118 and 0.12 mg_{PGM}/cm^2, respectively; 0.15mg_{Pt}/cm^2 Pt/NSTF cathode data included for reference. (b) Comparison of specific activity and specific area of conditioned and 30k cycled pretreated Pt_3Ni_7/NSTF, with conditioned Pt/NSTF for reference. (c) Activity and surface area metrics for two pretreated 0.12 mg_{PGM}/cm^2 Pt_3Ni_7/NSTF cathode MEAs evaluated under the U.S. DRIVE electrocatalyst cycle durability test.

While the pretreated Pt_3Ni_7/NSTF catalyst boasts high activity and improved limiting current density, rapid degradation occurred during fuel cell cycling tests in membrane electrode

assemblies.[21] This is demonstrated in Fig. 1b, where the Pt_3Ni_7/NSTF cathode shows significantly lower specific activity after 30k cycles. Much of the performance loss occurs in the first 10k cycles (Fig. 1c). This is attributed to the ongoing dealloying of Ni, as the large drop in mass activity is mostly a result of specific activity losses. The electrochemically active surface area is also negatively impacted, but not to the degree of the specific activity, which rapidly drops to the performance regime of pure Pt. Thus, although these transition-metal alloy catalysts are highly attractive due to their high initial performance, understanding the nature of these evolving structures within the fuel cell environment is critical to designing and modifying pretreatment protocols with the ultimate aim to create a catalyst with both high activity and durability.

Evolving Catalyst Morphology

The as-deposited Pt_3Ni_7/NSTF catalyst roll good, shown in Fig. 2, consists of a high density of individual catalyst-coated perylene-red whiskers. The continuous metal coating is made up of individual grains on the order of 10 nm in diameter (Table I). Dealloying and annealing pretreatments were performed on the roll good prior to transfer into catalyst coated membranes (CCMs). The net effect of the pretreatments was an increase in grain size and Pt mole fraction (Table I). Despite the higher Pt content, the alloy lattice parameter of the pretreated catalyst decreased slightly relative to the baseline. While this phenomena has yet to be fully explored, it is likely the results of improved alloy homogeneity as a consequence of the annealing pretreatment. High-angle annular dark-field (HAADF) STEM imaging was employed to study the catalyst surfaces. In this imaging mode, the intensity varies proportionally with the mass (Z-contrast) and the thickness of the analysed area. The images presented in Fig. 3b show the emergence of a Pt-skin structure following the pretreatments, as evidenced by the thin, high contrast layer along the grain surfaces. While such surface structures can be important to catalyst activity, the electrochemical results in Fig. 1 suggest they are of little consequence. Indeed, in order to play a role in catalyst activity, these structures must survive membrane electrode assembly and the lengthy conditioning process.

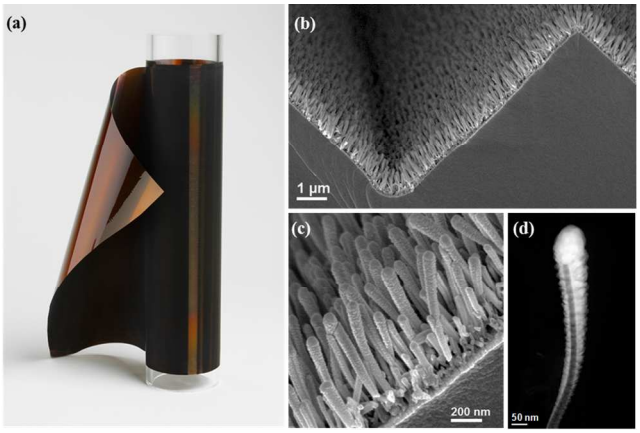

Fig. 2 (a) Photograph of a NSTF roll good, (b,c) SEM images of Pt_3Ni_7/NSTF on growth substrate, and (d) STEM-HAADF image of individual Pt_3Ni_7/NSTF whisker.

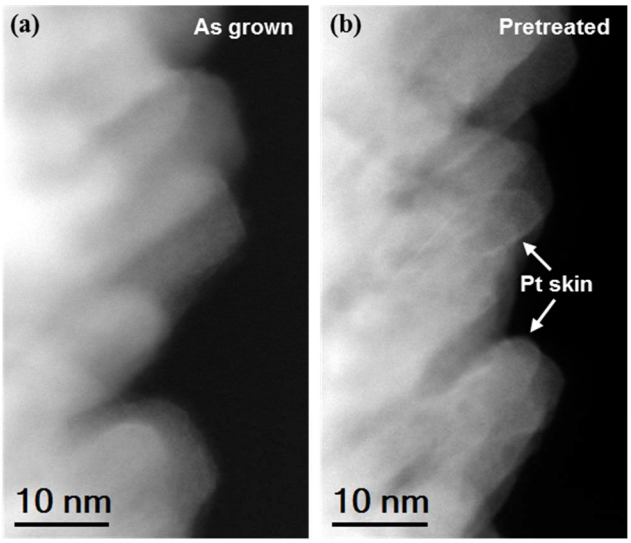

Fig. 3 HAADF-STEM images of (a) as-grown and (b) pretreated Pt_3Ni_7/NSTF showing the emergence of discontinuous Pt-skin structures.

NSTF Catalyst	Pt Content (mg/cm^2)	Pt Mole Fraction (%)	FCC (111) Grain Size nm	FCC Lattice Constant (Å)
Pure Pt	0.15	100	9.9	3.928±0.002
Pt_3Ni_7	0.12	34	9.6	3.696±0.003
Pretreated Pt_3Ni_7	0.118	42	10.8	3.693±0.002

Table I Metrics of as-grown and pretreated Pt_3Ni_7/NSTF showing slight changes in grain size and composition as a result of chemical dealloying and annealing. Pt/NSTF included for comparison.

Following pretreatment, the catalyst was transferred via a roll-to-roll process onto membranes to form CCMs, and then assembled into MEAs for electrochemical characterization and testing. Prior to mass activity, specific activity, and specific area measurements, the MEAs were conditioned to activate and stabilize the fuel cell. For Pt-nanoparticle catalysts, the conditioning process is usually less than 24 hours, while a more extensive process (40-60 hrs) is required for the NSTF catalyst.[12,22] The NSTF protocol involves the thermal cycling of the fuel cell, regularly switching between operational and cooldown states until stable performance is achieved.[22] Significant changes to the catalyst morphology as a result of conditioning are shown in Fig. 4. The formation of nanopores, which occurs as a consequence of Ni dissolution, was accompanied by large shift in alloy composition to Pt_7Ni_3, as determined by energy dispersive X-ray spectroscopy (EDS). It should be noted that this new composition is similar to the Pt_3M (M=Co,Ni,Fe) bulk films used by Stamenkovic to study highly active Pt-skin and skeleton surface structures[23] and $Pt_{1-x}N_x$ (x=0.25-0.30) dealloyed nanoparticles studied by Snyder et al.[3] In the latter work, the peak catalyst activity was attributed to a

combination of optimal residual Ni content (around 25-30 at.%) and porous structure formation following dealloying, where particle diameters must typically be greater than 15 nm for pore formation to occur. The average grain diameter for the NSTF catalysts is about 10 nm prior to conditioning (Table I), and TEM characterization suggested that the grain size increases further with conditioning, although this was difficult to quantify. Since regions of high Ni content will appear darker and can be misinterpreted as pores in STEM-HAADF images,[24] complementary secondary electron (SE) imaging was employed to observe the catalyst surfaces. The porous surfaces shown in the SE-STEM image in Fig. 4b confirm the contrast in the HAADF-STEM is a result of nanoporosity, with an average pore diameter of approximately 5 nm. As pore formation in nanoparticle systems can be controlled to some extent by modifying particle diameter and composition,[3,12,25] this key discovery is driving the modification of pretreatment protocols which aim to control porosity formation in NSTF by modifying alloy compositions and grain sizes.

It should also be noted that nanoporosity has been shown to have a negative impact on durability.[12,13] Thus, in this and ongoing studies, the promotion of high activity, high surface area structures is always considered in the context of durability. Shown in Fig. 4c is the morphology of the individual NSTF whisker following 30k fuel cell cycles. The Ni-depleted structure shows a significant increase in pore size. The additional change in alloy composition from 30 at.% Ni to 15 at.% Ni can partially account for the large loss in specific activity. Since changes in surface and near-surface composition can play an even more significant role in specific activity, electron energy loss spectroscopy (EELS) was employed to map the surfaces of the nanostructured thin films, as shown in Fig. 5. This technique was selected as the formation of ultrathin (monolayer) Pt-rich surface structures have been identified on alloy nanoparticles by atomic-resolution electron energy loss spectrum imaging previously.[4,11,26,27] In the pretreated catalyst, a very thin Pt skin layer was observed, as shown by the map and linescan in Fig. 5a,e. However, the thin skin layer was not observed in all regions, as shown by the map in Fig. 5b. In all cases, the alloy surface was covered by a thin Ni-oxide layer, which most likely forms during the heat treatment. Neither the oxide layer nor intermittent Pt skin structures have significant influence on catalyst performance due to the extensive compositional and structural changes during conditioning.

Following conditioning, the bulk alloy underwent a dramatic change in composition from Pt_3Ni_7 to Pt_7Ni_3. Further, EELS spectrum imaging showed that a Pt-rich surface layer, typically ranging from 1 to 1.5 nm had formed over the bulk alloy (Fig. 5c,f), Surface Ni readily dissolves in the acidic environment, such that a Pt-rich surface layer would be expected to form as Ni leaves the structure. The underlying alloy composition appeared highly non-homogeneous, which would suggest a high variation in catalyst activity from region to region. The large change in composition during conditioning suggests different starting alloy compositions and/or more aggressive pretreatments might be utilized to develop a catalyst with similar activity and surface area, but greatly improved durability within the fuel cell environment.

The aggressive drive cycling protocol transformed the highly active conditioned catalyst into a catalyst with specific activity more reminiscent of pure Pt. EELS maps of the whisker surfaces show a phase-separated alloy of mainly Pt with intermittent Ni-rich pockets (Fig. 5d,g). Electron diffraction found an increase in the lattice constant approaching that of pure Pt, which, when coupled with the EELS maps, suggests much of the strain and/or ligand effects have been lost. Thus, it is little surprise that the cycled catalyst behaves similar to pure Pt in electrochemical tests. It is surprising that the Pt skins observed following conditioning do not provide better protection against additional Ni dealloying. However, a similar phenomenon was observed for PtNi and PtCo nanoparticles, where non-porous catalysts exhibited much improved durability over porous conterparts.[12,13]

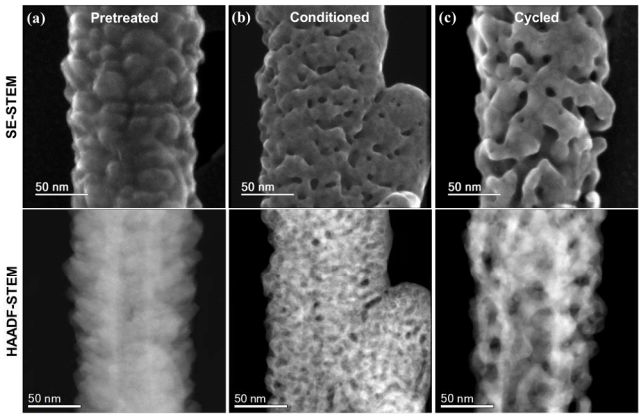

Fig. 4 Secondary-electron and HAADF STEM image pairs of (a) pretreated, (b) conditioned, and (c) cycled Pt_3Ni_7/NSTF. Conditioning results in the formation of nanoporosity, which grows with fuel cell cycling.

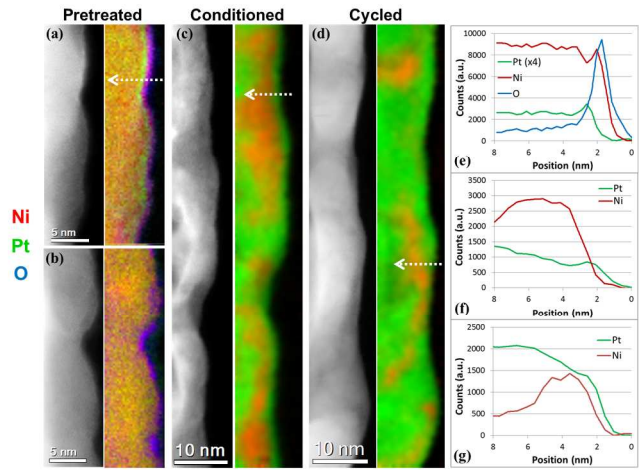

Fig. 5 HAADF-STEM image with EELS spectrum image and extracted line scan for (a,b,e) pretreated, (c,f) conditioned, and (d,g) cycled Pt_3Ni_7/NSTF.

As expected from the observed reduction in limiting current density, leached Ni ions were detected by EDS throughout the

polymer electrolyte membrane. Unlike dissolved Pt^{2+}, which is reduced by crossover hydrogen to form the well-studied Pt-band within the membrane,[28,29] the leached Ni remains as individual cations. A discernible band of Pt particles was not observed in the membrane, nor was Pt detected anywhere in the membrane or gas diffusion layer. This suggests Pt dissolution is immediately followed by redeposition onto the cathode, which further contributes to dissolution of underlying Ni and alloy inhomogeneity.

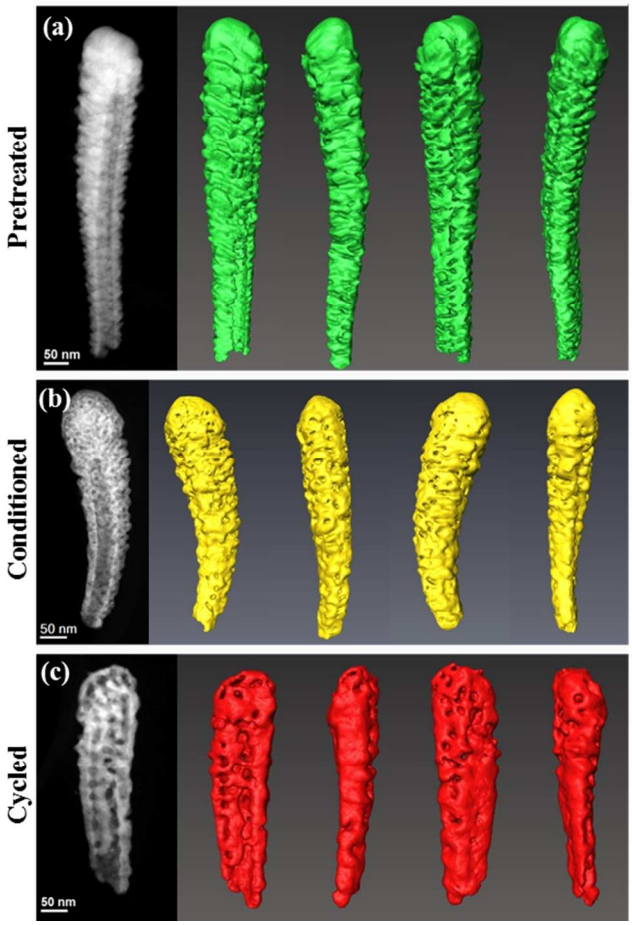

Fig. 6 HAADF-STEM images with orthogonal view of the rendered surfaces of individual (a) pretreated, (b) conditioned, and (c) cycled whiskers

Electron Tomography

To further investigate the porous structure of the NSTF catalyst, three-dimensional reconstructions of individual pretreated, conditioned, and drive cycled whiskers were created using electron tomography techniques, multiple views of which are presented in Fig. 6. Videos of the reconstructions are available in the supplemental material.

The multiple views of the pretreated whisker (Fig. 6a) show the "lath" shape identified by Debe et al.[30] The nanostructured "whiskerette" morphology of the alloy NSTF catalyst is apparent, exhibiting enhanced growth along certain facets arising from surface steps on the crystalline perylene-red. The tomographic reconstructions of the conditioned and cycled whisker show the complex network of pores (Fig. 6a,b). Note that the 3D nature of the pore network is difficult to interpret from two-dimensional TEM images, and can be only be fully resolved using nm-scale electron tomography. The reconstruction also shows a general smoothing of the whisker surface as a result of conditioning, which is further increased with potential cycling. The conditioned and cycled whiskers examined here were shorter than the annealed whisker, suggesting possible whisker fragmentation induced by the thermal and electrochemical cycling processes and/or by mechanical cleavage during the ultrasonication sample preparation procedure.

Individual cross-sectional slices extracted from the reconstructed volume in the directions parallel and perpendicular to the electron probe provide valuable insight into the degree and depth of porosity formed following conditioning and cycling (Fig. 7). It becomes evident that many of the pores in the conditioned whisker extend to the perylene-red core and are, in some cases, interconnected with other pores. This is further demonstrated in the segmented data set in Fig. 8, showing the pore+core volume in blue for each whisker. After aging, the pore size increases dramatically, to the extent that the whisker core can be readily observed.

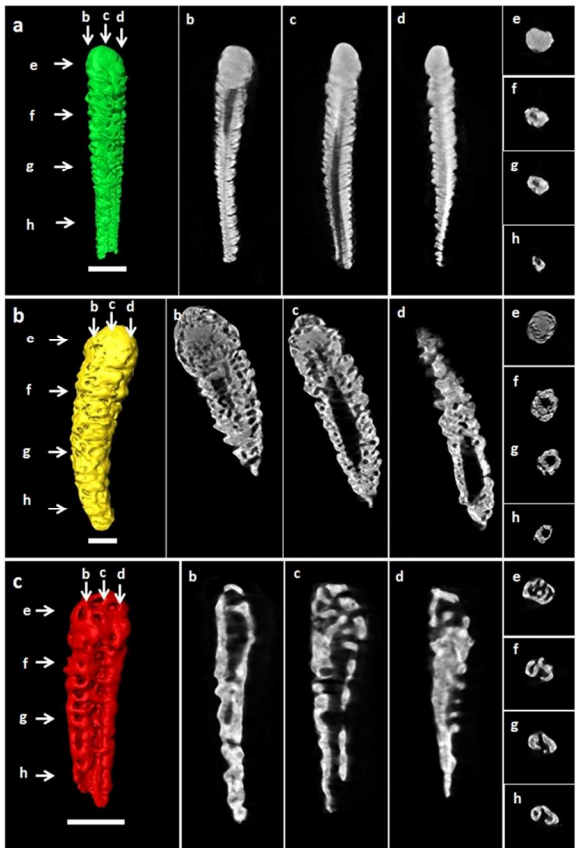

Fig. 7. 3D rendered surface of a representative (a) pretreated, (b) conditioned, and (c) cycled NSTF whiskers. Series of individual cross-sectional slices extracted from the reconstructed volume in the direction parallel (b-d) and perpendicular to the probe (e-h). The scale bars correspond to 100 nm

From these segmentations, the NSTF alloy catalyst surface area and alloy volume for each whisker were quantified and are summarized in Table II. Since the alloy compositions were previously measured by EDS, the nominal Pt loading for each whisker could be calculated. Through the combination of electron tomography and EDS quantification, the specific surface area of each whisker was estimated.

A two-fold increase in the ratio of alloy surface area to volume was observed as a result of catalyst conditioning due to the high porosity of the conditioned catalyst. The estimated specific area of the conditioned catalyst (12.2 m^2/g_{Pt}) was close to the experimental bulk value (14.7 m^2/g_{Pt}), as determined by cyclic voltammetry. This result shows that the much higher specific area of the Pt_3Ni_7/NSTF catalyst over the more conventional Pt/NSTF can be attributed to the formation of a nanoporous structure formed by *in situ* Ni leaching during conditioning.

The tomographically-determined specific area of the cycled whisker dropped by a factor of 4x, which is surprising considering the bulk specific area only dropped by 1.45x. However, it is possible that with extended cycling, the core of the whisker may also become accessible for the ORR. This is not altogether unexpected, as sublimation of the perylene-red core was observed during annealing in H_2 and after severe potential cycling.[10,31] By factoring in the whisker core into the surface area calculations, the new calculated specific area (cycled+interior) of 8.3 m^2/g_{Pt} scales appropriately with the bulk value (10.1 m^2/g_{Pt}). Not only does this indicate that the whisker core may contribute to the specific area upon extended cycling, but also suggests a new path for further increasing the specific area of NSTF in future catalyst pretreatment experiments.

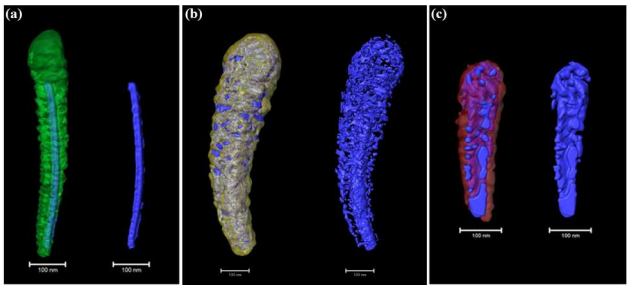

Fig. 8. 3D segmentation of the alloy whiskers and core/pore volume for the (a) annealed (b) conditioned, and (c) cycled whiskers used for calculating alloy surface area, alloy volume, and specific area in Table II.

Stage	Length (nm)	Alloy Surface Area (nm^2)	Alloy Volume (nm^3)	SA:V	Alloy Comp.	PGM (g)	Specific Area (m^2/g_{Pt})	Bulk Specific Area (m^2/g_{Pt})
Pretreated	650	2.8E+05	2.6E+06	0.108	Pt_4Ni_6	2.5E-14	--	--
Conditioned	443	3.4E+05	1.6E+06	0.216	Pt_7Ni_3	2.5E-14	12.2	14.7
Cycled	413	6.9E+04	1.3E+06	0.054	Pt_8Ni_2	2.3E-14	3.1	10.1
Cycled+interior	413	1.8E+05	1.3E+06	0.142	Pt_8Ni_2	2.3E-14	8.3	10.1

Table II. Alloy surface area and volume quantified from 3D segmentations. These values combined with catalyst composition quantified by EDS allowed for an estimation of the specific area, which is compared with bulk values.

Conclusions

In summary, a series of highly active Pt_3Ni_7/NSTF catalysts were characterized following dealloying and annealing pretreatments on the growth substrate and conditioning and drive cycling within MEAs. It was discovered that fuel cell conditioning played a dominate role in generating the morphological and compositional characteristics which determine catalyst performance. The high surface area of the cathode catalyst was found to be the result of substantial Ni dissolution, which led to the formation of small pores within the NSTF layer. The high specific activity was attributed to a concomitant change in the alloy composition from Pt_3Ni_7 to Pt_7Ni_3 and the formation of 1 to 1.5 nm-thick Pt-rich surface layer.

Drive cycling was also performed to investigate the durability of the structures formed during catalyst conditioning. After 30k cycles, only 15 at.% Ni remained in the NSTF alloy cathode. Pore size and surface smoothing increased substantially as the Pt skin layer formed during conditioning was unable to protect subsurface Ni from further dissolution. These nanoscale changes resulted in significant specific activity and specific area losses.

It was also demonstrated that the surface area, volume, Pt loading, and specific area could be estimated for individual NSTF catalyst whiskers using a combination of EDS quantification and electron tomography. These values were correlated with cyclic voltammetry measurements to confirm that the high surface area of the catalyst is indeed a result of nanoporosity formed during conditioning. It was further suggested that upon drive cycling, the whisker core may contribute new Pt active sites for the ORR.

These findings highlight the importance of characterizing the catalyst in the same state as activity measurements in order to establish accurate structure-property relationships. Future studies will utilize different alloy compositions to determine the subsequent impact on nanoporostiy and Pt-skin thickness. More aggressive dealloying and annealing procedures will also be developed with the aim to create a more stable catalyst while further extending gains in ORR activity.

Experimental Section

Synthesis and Electrochemical Evaluation

Pt_3Ni_7/NSTF catalysts were fabricated using roll-to-roll continuous pilot-scale production equipment. Pt_3Ni_7/NSTF catalysts were first generated by sputter deposition from a single Pt_3Ni_7 alloy target onto an NSTF support roll-good via pilot production equipment; the Pt content per electrode surface area was 0.12 mg_{Pt}/cm^2. The Pt_3Ni_7/NSTF was then submitted to a pretreatment process, consisting of exposing the Pt_3Ni_7/NSTF roll-good through a 3M proprietary chemical treatment bath, after which the catalyst was rinsed and dried prior to passing through a 3M proprietary surface energetic treatment (SET) annealing process. Catalyst samples were

analyzed for Pt and Ni content by X-ray fluorescence (XRF). Grain sizes and lattice constants were measured via X-ray diffraction (XRD).

Electrodes were assembled into CCMs, and were then submitted to a conditioning process to activate the fuel cell, after which electrochemical measurements were recorded and cyclical voltage testing was performed.[13,22] 50 cm^2 CCMs containing the as-deposited, dealloyed, annealed Pt_3Ni_7/NSTF cathodes were fabricated with 3M 825EW 24 μm thick perfluorosulfonic acid (PFSA) PEMs and either 0.05 mg_{PGM}/cm^2 PtCoMn/NSTF or 0.03 mg_{PGM}/cm^2 Pt/NSTF anodes. CCMs were installed in 50 cm^2 Fuel Cell Technologies quad-serpentine flow field test cells with 3M 2979 GDLs at 10% strain. After initial conditioning, these membrane electrode assemblies (MEAs) were evaluated for cathode ORR mass activity (80°C, 150kPa H_2/O_2, 100% RH, $0.900V_{Meas}$, 1050s hold), specific Pt surface area via integration of cyclic voltammetry-determined HUPD charge divided by 220 $\mu C/cm^2_{Pt}$ (70°C, 100kPa H_2/N_2, 100% RH, 100mV/s), and H_2/Air Performance via polarization curves (80°C, 150 kPa H_2/Air, 68°C dewpoints, constant H_2/Air stoichiometry of 2.0/2.5). Additional details of MEA fabrication and 3M fuel cell measurements can be found in Ref. 20. MEAs with the dealloyed and annealed Pt_3Ni_7/NSTF cathodes were also evaluated for durability under the USCAR Fuel Cell Tech Team Electrocatalyst Durability cycle,[32] consisting of 30,000 50 mV/s cycles between 0.6-1.0 V at 80°C, 100 kPa H_2/N_2, 800/1800SCCM, 100% RH. ORR activity, specific surface area, and H_2/Air performance were evaluated at beginning of life and after 10, 20, and 30 thousand cycles.

STEM Characterization

In preparation for STEM analysis, NSTF whiskers were removed from the either the growth substrate or MEA by sonication in methanol, then dropcast onto a lacey carbon film. Thin cross-sections of catalyst coated membranes (CCMs) were also prepared by diamond-knife ultramicrotomy. STEM high-angle annular dark-field (HAADF) imaging and energy dispersive X-ray (EDS) analysis was performed in a JEOL JEM2200FS operated at 200 kV and equipped with a third-order CEOS aberration corrector and Bruker XFlash silicon drift detector. Lattice parameter measurements were performed by selective area electron diffraction (SAED) in a HF3300 TEM/STEM. Electron energy loss spectrum images were recorded in a Nion UltraSTEM 100 operated at 100keV and equipped with a Gatan Enfina spectrometer. Spectrum images were recorded with a pixel dwell time or 0.15 s and dispersion of 0.5 ev/ch. Spectrum images were denoised using the spectral decomposition routine in the Hyperspy software suite. STEM-HAADF electron tomography was carried out on a LB FEI TITAN 80-300 electron microscope equipped with a probe Cs-corrector operating at 200 kV and using a Fischione 2020 single-tilt tomography holder. Aberrations of the condenser lenses were corrected up to second-order using the Zemlin tableau. A convergence angle of 10 mrad and 130 mm of camera length were used. Using the "3D Explorer" FEI software, the data collections were performed by tilting the specimen around a single axis perpendicular to the electron beam between -72° and +72°. In order to reconstruct tomograms, the registered tilt series were aligned using the FEI Inspect 3D software and an in-house software written in MATLAB. In particular, SIRT algorithms, using 30 iterations, were applied. The reconstructed volumes were thereafter processed using the Avizo 6.0 Fire edition and the Fiji software. In particular, automated thresholding was carried out using Otsu algorithm, providing a good correspondence to the NSTF whiskers.

Acknowledgements

This work was supported by the Fuel Cell Technologies Office, Office of Energy Efficiency and Renewable Energy, U.S. Department of Energy under Award Number DE-EE0005667 and through a user project supported by ORNL's Center for Nanophase Materials Sciences (CNMS), which is a DOE Office of Science User Facility.

Notes and references

[a] Materials Science and Technology Division, Oak Ridge National Laboratory, Oak Ridge, TN, 37830, USA.
[b] CEA, INAC, 38054 Grenoble cedex 9, France.
[c] CEA, LITEN, 38054 Grenoble cedex 9, France.
[d] Fuel Cell Components Program, 3M Co. 201-2N-19, 3M Center, St. Paul, Minnesota 55144-1000.

† Retired

Electronic Supplementary Information (ESI) available: Videos of tomographic reconstruction of NSTF whiskers. See DOI: 10.1039/b000000x/

1 M. K. Debe, *Nature*, 2012, **486**, 43-51.
2 V. R. Stamenkovic, B. S. Mun, M. Arenz, K. J. J. Mayrhofer, C. A. Lucas, G. P. Wang, N. Ross, N. M. Markovic, *Nat. Mater.*, 2007, **6**, 241-247.
3 J. Snyder, I. McCue, K. Livi, J. J. Erlebacher, *Am. Chem. Soc.*, 2012, **124**, 8633-8645.
4 L. Gan, M. Heggen, S. Rudi, P. Strasser, *Nano Lett.*, 2012, **12**, 5423-5430.
5 C. Chuy, M. Davis, M. Guenther, H. Hass, D. Susac, C. Talpalaru, H. Zhang, *ECS Trans.*, 2013, **50**, 1563-1573.
6 M. K. Debe, *J. Electrochem. Soc.*, 2013, **160**, F522-F534.
7 M. Hara, M. Lee, C. H. Liu, B. H. Chen, Y. Yamashita, M. Uchida, H. Uchida, M. Watanabe, *Electrochim. Acta*, 2012, **70**, 171-181.
8 M. K. Debe, A. J. Steinbach, G. D. Vernstrom, S. M. Hendricks, M. J. Kurkowski, R. T. Atanasoski, P. Kadera, D. A. Stevens, R. J. Sanderson, E. Marvel, J. R. Dahn, *J. Electrochem. Soc.*, 2011, **158**, B910-B918.
9 D. A. Stevens, R. Mehrotra, R. J. Sanderson, G. D. Vernstrom, R. T. Atanasoski, M. K. Debe, J. R. Dahn, *J. Electrochem. Soc.*, 2011, **158**, B905-B909.

10 D. F. van der Vliet, C. Wang, D. Tripkovic, D. Strmcnick, X. F. Zhang, M. K. Debe, R. T. Atanasoski, N. M. Markovic, V. R. Stamenkovic, *Nat. Mater.*, 2012, **11**, 1051-1058.
11 L. Gan, M. Heggen, R. O'Malley, B. Theobald, P. Strasser, *Nano Lett.*, 2013, **13**, 1131-1138.
12 B. Han, C. E. Carlton, A. Kongkanand, R. S. Jukreja, B. R. Theobald, L. Gan, R. O'Malley, P. Strasser, F. T. Wagner, Y. Shao-Horn, *Energy Environ. Sci.*, 2015, **8**, 258-266.
13 Q. Jia, K. Caldwell, K. Strickland, J. M. Ziegelbauer, Z. Liu, Z. Yu, D. E. Ramaker, S. Mukerjee, *ACS Catal.*, 2015, **5**, 176-186.
14 M. Zhiani, S. Majidi, *Int. J. Hydrogen Energ.*, 2013, **38**, 9819-9825.
15 Z. Qi, A. Kaufman, *J. Power Sources*, 2003, **114**, 21-31.
16 Z. Xu, Z. Qi, C. He, A. Kaufman, *J. Power Sources*, 2006, **156**, 315-320.
17 D. E. Ramaker, A. Korovina, V. Croze, J. Melke, C. Roth, *Phys. Chem. Chem. Phys.*, 2014, **16**, 13645-13653.
18 Q. Jia, K. Caldwell, D. E. Ramaker, J. M. Ziegelbauer, Z. Liu, Z. Yu, M. Trahan, S. Mukerjee, *J. Phys. Chem. C*, 2014, **118**, 20496-20503.
19 T. Okada, H. Satou, M. Okuno, M. Yuasa, *J. Phys. Chem. B*, 2002 **106**, 1267-1273
20 B. L. Kienitz H. Baskaran, T. A. Zawodzinski, Electrochim. Acta, **54**, 2009, 1671-1679.
21 K. M. Caldwell, D. E. Ramaker, Q. Jia, S. Mukerjee, J. M. Ziegelbauer, R. S. Kukreja, A. Kongkanand, *J. Phys. Chem. C*, 2015, **119**, 757-765.
22 A. J. Steinbach, C. V. Hamilton, Jr., M. K. Debe, *ECS Trans.*, 2007, **11**, 889-902.
23 V. R. Stamenkovic, B. S. Mun, K. J. J. Mayrhofer, P. N. Ross, N. M. Markovic, *J. Amer. Chem. Soc.*, 2006, **128**, 8813-8819.
24 Z. Liu, H. Xin, Z. Yu, Y. Zhu, J. Zhang, J. A. Mundy, D. A. Muller, F. T. Wagner, *J. Electrochem. Soc.*, 2012, **159**, F554.
25 J. Erlebacher, M. J. Aziz, A. Karma, N. Dimitrov, K. Sieradzki, *Nature*, 2001, **410**, 450-453.
26 H. L. Xin, J. A. Mundy, Z. Liu, R. Cabezas, R. Hovden, L. F. Kourkoutis, J. Zhang, N. P. Subramanian, R. Makharia, F. T. Wagner, D. A. Muller, *Nano. Lett.*, 2012, **12**, 490-497.
27 M. Lopez-Haro, L. Dubau, L. Guetaz, P. Bayle-Guillemaud, M. Chatenet, J. Andre, N. Caque, E. Rossinot, F. Maillard, *Appl. Catal. B-Environ.*, 2014, **152**, 300–308.
28 P. J. Ferreira, G. J. la O', Y. Shao-Horn, D. Morgan, R. Makharia, S. Kocha, H. A. Gasteiger, *J. Electrochem. Soc.*, 2005, **152**, A2256-A2271.
29 W. Bi, G. E. Gray, T. F. Fuller, *Electrochem. Sol. St.*, 2007, **10**, B101-B104.
30 M. K. Debe, A. R. Drube, *J. Vac. Sci. Technol. B*, 1995, **13**, 1236-1241.
31 V. Lee, D. Susac, S. Kundu, V. Berejnov, R.T. Atanasoski, A.P. Hitchcock, J. Stumper, *ECS Trans.*, 2013, **58**, 473-479.
32 U.S. DRIVE Partnership Fuel Cell Technical Team "Cell Component Accelerated Stress Test and Polarization Curve Protocols for Polymer Electrolyte Membrane Fuel Cells", Revision Dec. 2010, Table I, http://www.uscar.org/commands/files_download.php?files_id=267 (Sept. 2013).

High resolution imaging and electron tomography are used to link nanoscale morphology with electrochemical activity in highly active Pt_3Ni_7 nanostructured thin film catalysts, revealing the critical role of catalyst conditioning.